nature physics

Article

https://doi.org/10.1038/s41567-024-02617-7

Observation of chiral edge transport in a rapidly rotating quantum gas

Received: 2 February 2024

Accepted: 23 July 2024

Published online: 6 September 2024

Check for updates

Ruixiao Yao, Sungjae Chi, Biswaroop Mukherjee, Airlia Shaffer, Martin Zwierlein & Richard J. Fletcher

The frictionless directional propagation of particles at the boundary of topological materials is a striking transport phenomenon. These chiral edge modes lie at the heart of the integer and fractional quantum Hall effects, and their robustness against noise and disorder reflects the quantization of Hall conductivity in these systems. Despite their importance, the controllable injection of edge modes, and direct imaging of their propagation, structure and dynamics, remains challenging. Here we demonstrate the distillation of chiral edge modes in a rapidly rotating bosonic superfluid confined by an optical boundary. By tuning the wall sharpness, we reveal the smooth crossover between soft wall behaviour in which the propagation speed is proportional to wall steepness and the hard wall regime that exhibits chiral free particles. From the skipping motion of atoms along the boundary we infer the energy gap between the ground and first excited edge bands, and reveal its evolution from the bulk Landau level splitting for a soft boundary to the hard wall limit. Finally, we demonstrate the robustness of edge propagation against disorder by projecting an optical obstacle that is static in the rotating frame.

After the discovery of the integer quantum Hall effect[1], it was quickly realized that the remarkable quantization of electrical conductivity could be viewed as due to either states extending through the entire bulk[2] or the universal contribution of an integer number of edge channels[3]. This equivalence is an example of bulk–edge correspondence that relates the occurrence, number and nature of edge modes to topological invariants in the bulk[4–7]. It was subsequently discovered that edge modes are in fact ubiquitous at the boundary of a much wider class of topological materials, making them central to the physics of fractional quantum Hall[8] and spin Hall[9] fluids, topological insulators[7], photonic platforms[10] and exotic superfluids[11] and superconductors[12].

Despite this theoretical universality, the intricate interplay between edge disorder, interparticle interactions and wall geometry in real materials can profoundly modify the spatial structure, speed and even direction of edge transport[13–19]. This results in non-universal behaviour and obscures the fundamental underlying physics. It is therefore crucial to realize clean, tunable platforms in which we can controllably explore edge physics, as well as tools for the direct microscopy of their structure and dynamics. However, this is challenging in condensed matter platforms, as available probes do not resolve down to the magnetic length scale[20–24], have restricted spatial extent[25,26] or feature unwanted probe–sample coupling[27], and control over wall geometry is difficult.

Ultracold quantum gases in artificial magnetic fields[28,29] provide an enticing arena for exploring edge transport. Gauge fields have been generated via spin–orbit coupling[29–31], phase imprinting in lattices[32–37] and rotation of the trapped gas[38–42]. The latter approach uses the analogy between the Lorentz force on a charged particle in a magnetic field and the Coriolis force on a particle of mass m in a frame rotating at frequency Ω, yielding rotational analogues of the cyclotron frequency $\omega_c = 2\Omega$ and magnetic length $\ell_B = \sqrt{\hbar/(m\omega_c)}$. Furthermore, in contrast to fermionic electrons that fill all states below the Fermi energy, bosonic atoms in the mean-field quantum Hall regime[43] all occupy a single wavefunction, whose dynamics offers microscopic insight into the individual building blocks of quantum Hall systems. Chiral motion under a gauge field has been observed in lattices with synthetic

MIT-Harvard Center for Ultracold Atoms, Research Laboratory of Electronics and Department of Physics, Massachusetts Institute of Technology, Cambridge, MA, USA. e-mail: rfletch@mit.edu

https://doi.org/10.1038/s41567-024-02617-7

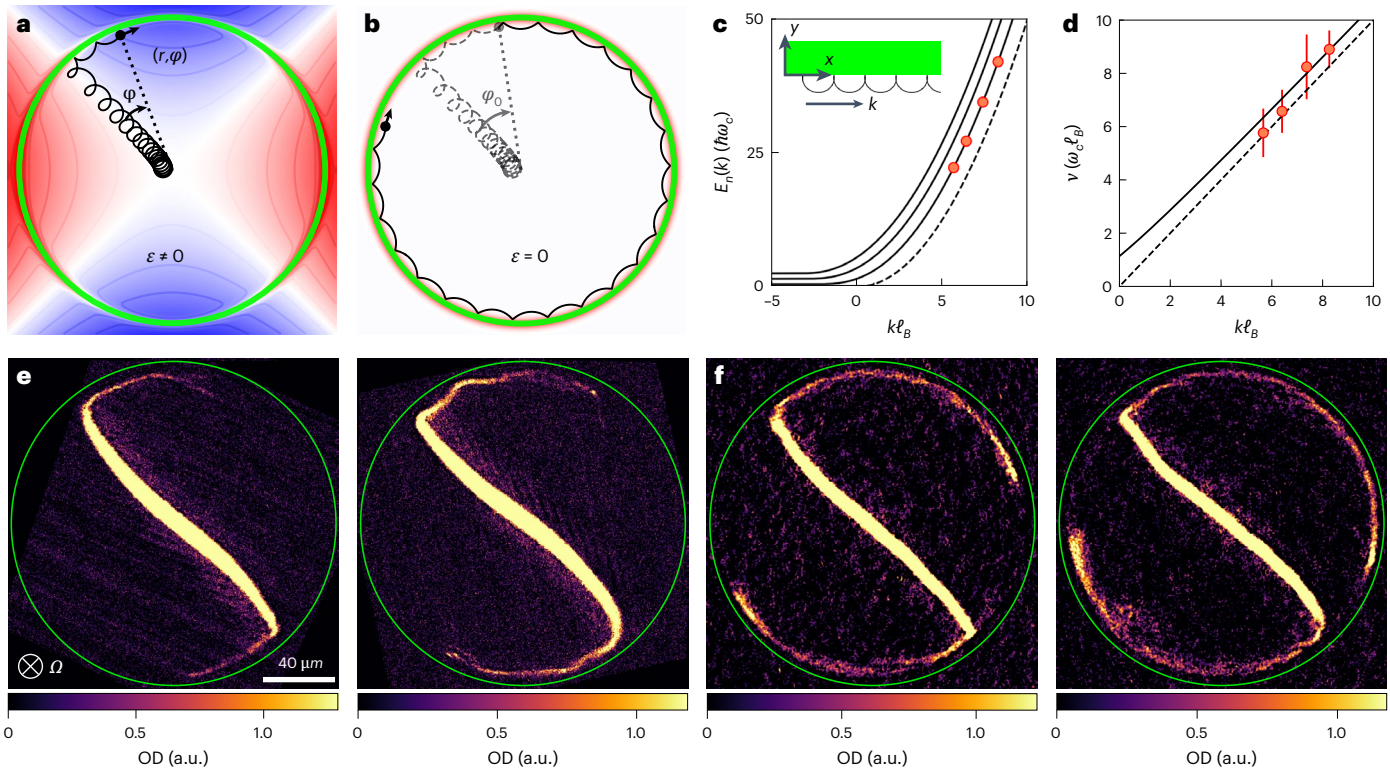

Fig. 1 | Controllable injection of chiral edge modes. a, In the frame rotating at Ω, atoms experience an artificial magnetic field, a scalar saddle potential (red/blue contours) of strength ε and a sharp confining wall (green). The black line shows a classical trajectory, exhibiting radially drifting cyclotron orbits[41] followed by chiral skipping motion along the boundary. **b**, After atoms have propagated by a variable azimuthal angle φ_0, we turn off the saddle potential, freezing the momentum $\hbar k$ of the edge mode wavefront, which subsequently propagates at a constant speed. **c**, The dispersion relation $E_n(k)$ associated with a hard wall for the lowest three bands $n = 0, 1, 2$ (black lines)(ref. 47). For large k, these are approximately captured by the chiral free-particle energy $\hbar^2k^2/(2m)$ (dashed line). The red data points indicate the wavevectors of atoms at the wavefront, corresponding to four different values of φ_0.The inset shows the orientation of the repulsive wall (green), the edge mode wavevector k, and the spatial coordinates x and y. **d**, The edge mode group velocity as a function of k, where the dashed line shows the speed $\hbar k/m$ of chiral free particles. The solid line shows the speed obtained from the lowest band $E_0(k)$. Error bars indicate 1σ. **e**, The measured density distribution after propagation of the edge mode for approximately 5 ms (left) and 9 ms (right) in the presence of the saddle. OD, optical density; a.u., arbitrary units. **f**, The measured edge mode density after propagation for 15 ms in the presence of the saddle, and then for 5 ms (left) and 8 ms (right) in its absence.

dimensions formed by an internal state manifold[31,35–37,44]. However, exploring the role of interactions and wall structure is difficult in these systems.

Here we realize the distillation of chiral edge modes at the boundary of a quantum gas subject to an artificial magnetic field, as illustrated in Fig. 1. The emergence of these modes is readily apparent. For a wall potential $V_{\mathrm{wall}}(y)$ that confines atoms to the region $y < 0$, it is convenient to work within the Landau gauge and label eigenstates by their wavevector k along the boundary, yielding a Hamiltonian:

$$\hat{H} = \frac{\hat{p}_y^2}{2m} + \frac{1}{2}m\omega_c^2\left(\hat{y} - k\ell_B^2\right)^2 + V_{\mathrm{wall}}(\hat{y}). \qquad (1)$$

Cyclotron motion of the atoms is reflected in an effective harmonic oscillator along the y direction of angular frequency ω_c. For $k \ll 0$, states are located far from the wall and their dispersion relation is flat, forming discrete Landau levels spaced by $\hbar\omega_c$. However, for $k \gg 0$ the position and momentum of states decouple. Atoms remain fixed at $y \approx 0$ and acquire an energy $\sim\hbar^2k^2/(2m)$, giving an approximately quadratic dispersion relation. As this occurs only for $k > 0$, the boundary hosts chiral free particles with a strictly positive group velocity $\hbar k/m$. This simple model underpins the chiral Fermi liquid of electrons at the boundaries of integer quantum Hall states[3], whereas strongly correlated fractional quantum Hall fluids instead support chiral Luttinger liquids[45].

The basic idea of our experiment is shown in Fig. 1. We prepared a condensate of 8×10^5 atoms of ^{23}Na in a time-orbiting-potential trap[41,46] with a root mean squared radial frequency $\omega = 2\pi \times 88.6(1)$ Hz. In the reference frame rotating at $\Omega = \omega$, atoms experience an artificial magnetic field with $\omega_c = 2\omega$. A sharp boundary is provided by an azimuthally symmetric optical wall of radius $R = 90$ μm, formed by projecting a circular mask onto the atoms. Given that $R \gg \ell_B$, the curved wall may be considered as linear from the perspective of atomic dynamics described by the Hamiltonian of equation (1), with local coordinates $(\hat{\mathbf{x}}, \hat{\mathbf{y}})$ directed along and into the wall, respectively.

The injection and subsequent propagation of a chiral edge mode is illustrated in Fig. 1a,b, and corresponding images of the atomic density are shown in Fig. 1e,f. First, we drove a radial flow of atoms towards the wall via a rotating anisotropy of the underlying harmonic trap, meaning that in the rotating frame atoms experience a static scalar saddle potential $V_s = -\varepsilon m\omega^2 r^2 \sin 2\varphi/2$. Here $\varepsilon = 0.125(4)$ is the strength of the anisotropy and (r, φ) are radial and azimuthal coordinates. Isopotential flow in this saddle, in analogy to the $\mathbf{E} \times \mathbf{B}$ drift of electromagnetism, leads to a radial motion of atoms along the diagonal. Crucially, the energy of an atom in the vicinity of the edge increases with its wavevector k along the wall. The azimuthal impulse provided by the saddle therefore injects atoms into states with non-zero group velocity, and they begin to propagate along the boundary[31]. The wavevector of an atom evolves with its azimuthal position, with the leading edge of the density distribution corresponding to atoms with the highest injected wavevector.

https://doi.org/10.1038/s41567-024-02617-7

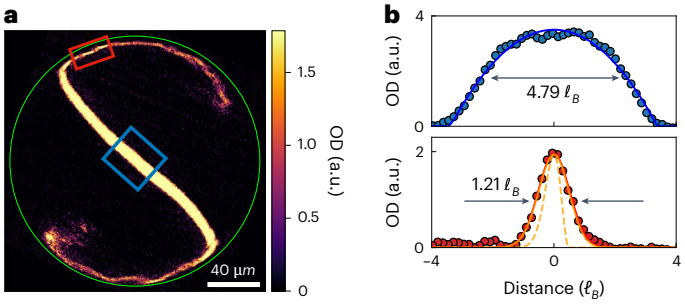

Fig. 2 | Density profiles of the bulk and edge modes. a, The density distribution imaged after 22 ms of edge mode propagation. **b**, The integrated transverse density profiles of the bulk condensate (top; blue box in **a**) and the injected edge mode (bottom; ref box in **a**). The blue curve shows a Thomas–Fermi function with a fitted FWHM ≈ 4.8 ℓ_B, indicating a Landau level occupation of ~6. The dashed orange line shows the theoretical density profile of the lowest-energy edge mode[47]. The solid orange line shows this profile convolved with a Gaussian characterizing the known effective resolution of our imaging system without any free parameters. For ease of comparison, the normalization was chosen such that the peak heights coincide, and the spatial origin of each plot was chosen to lie at the peak density.

Once this wavefront reaches a variable azimuthal angle, φ_0, we turned off the saddle potential, which freezes the momentum evolution. Subsequent propagation of the wavefront occurs at a constant group velocity, without detectable dissipation or backscattering.

The speed of an edge mode is determined by its associated dispersion relation. In Fig. 1c we show the theoretical dispersion relation $E_n(k)$ for a hard wall[47], where $n = 0, 1, 2\ldots$ labels discrete bands that connect to Landau levels in the bulk. The lowest band $E_0(k)$ approximately matches the quadratic dispersion relation $\hbar^2k^2/(2m)$ of a chiral free particle, shown by a dashed line. The red points indicate the injected edge mode corresponding to four values of φ_0. Here k is inferred by noting that the Hamiltonian in the rotating frame is time-independent, thus energy is conserved and atoms acquire kinetic energy as they move down the saddle potential (Methods). The corresponding measured edge mode speed is shown in Fig. 1d, where the solid line indicates the theoretical prediction $\hbar^{-1}\partial_k E_0(k)$ without any free parameters. The data are consistent with the propagation of chiral free particles at the boundary of our system, the speed of which $\hbar k/m$ is shown by the dashed line.

We note that according to the Ehrenfest theorem, the wavepacket dynamics observed here correspond closely to the motion of a classical particle, shown by a solid black line in Fig. 1a,b. However, in our experiment the spatial structure of the edge mode revealed that the atoms predominantly occupy the lowest band within a quantum mechanical description, whose size is limited by zero-point motion. To illustrate this, in Fig. 2 we show the transverse density profile of both the bulk and the edge modes. The bulk condensate density is described well by a Thomas–Fermi function with radius $R_{\mathrm{TF}} \approx 3.4\ \ell_B$ implying a chemical potential $\mu = (1/2)m\omega_c^2R_{\mathrm{TF}}^2 \approx 6\ \hbar\omega_c$ and hence that approximately six Landau levels are admixed into the superfluid wavefunction[42]. However, the edge mode shows a markedly different structure, with a Gaussian fit (red line) yielding a full-width at half-maximum (FWHM) of 1.21(2) ℓ_B. This indicates a size limited by the magnetic length, associated with the lowest edge band. The dashed orange line in Fig. 2b shows the theoretical density profile of a ground band edge mode with the average wavevector of atoms within the red region, while the solid orange line shows this profile blurred by the known effective resolution of our imaging system[41]. The agreement is excellent without any free parameters, indicating that the injected edge mode predominantly occupies the lowest band. This is consistent with the chemical potential ~$3\hbar\omega_c$ of the condensate within the red region, inferred from the atomic density, which is smaller than the splitting ~$6\hbar\omega_c$ between the ground and first excited bands obtained from the theoretical dispersion relation shown in Fig. 1c. For comparison, the FWHM of an edge mode in the first excited band would be ~1.5 ℓ_B when measured with our imaging system[41].

The data presented in Figs. 1 and 2 are captured well by a theoretical model assuming a hard wall. However, the geometry of the confining potential plays a crucial role in topological materials[14–19]. To address the effect of wall sharpness on the associated edge mode physics we intentionally defocused the objective used to project the optical boundary, and monitored the resulting intensity pattern using a focused second objective (Methods). We characterized the boundary by modelling it as a piecewise potential, $V_{\mathrm{wall}} = \alpha\hbar\omega_c y/\ell_B$ for $y > 0$ and zero when $y < 0$, where the dimensionless quantity α determines the effective steepness.

In Fig. 3a we show the azimuthal position of the edge mode wavefront as a function of propagation time, for $\alpha \approx 5$ and $\alpha \approx 24$, along with representative images of the atomic density. It is qualitatively apparent that the propagation speed along the steeper wall is greater. For these measurements the saddle potential is continually present, meaning that the edge mode momentum and group velocity vary symmetrically about $\varphi = \pi/4$, at which they attain their maximum values. We fitted these data with a sigmoid function, determined the peak angular speed and inferred the edge mode peak linear speed v. This is shown in Fig. 3b as a function of α, which we have corrected for the small outward force ~$1.8\ \hbar\omega_c/\ell_B$ arising from the saddle at $\varphi = \pi/4$.

The speed shows a pronounced crossover between linear behaviour $v \propto \alpha$ for shallow walls and saturating at a constant value as the steepness increases. This crossover may be understood by comparing the typical wavevector of an edge mode in our experiment to $\alpha\ell_B^{-1}$. If $k\ell_B \gg \alpha$, then atoms are located at $y \gg \ell_B$ and experience an approximately linear potential $\sim \hat{y} = \hat{Y} + \hat{\eta}$. Here $(\hat{\xi}, \hat{\eta})$ are the spatial coordinates associated with cyclotron motion, which occurs around the guiding centre $(\hat{X}, \hat{Y})$ (ref. 41). A linear potential therefore does not couple cyclotron and guiding centre coordinates regardless of its strength, and their dynamics remain independent. The guiding centres undergo isopotential drift at a speed $\alpha\omega_c\ell_B$ (ref. 41), implying an edge mode speed proportional to the wall sharpness, while the edge bands remain split by the bulk Landau level value $\hbar\omega_c$.

Conversely, if $0 \lesssim k\ell_B \lesssim \alpha$, then atoms are located at $|y| < \ell_B$ and a wavepacket of typical extent ~ℓ_B explores the force discontinuity at the onset of the wall, which mixes cyclotron and guiding centre motion. In the limit $\alpha \to \infty$ the wall does not provide any length or energy scale, implying a universal edge dispersion relation that depends only on $k\ell_B$ and ω_c.

In our experiment, using the free-particle dispersion relation $\hbar^2k^2/(2m)$ we estimated a typical maximum wavevector $k_{\max} \sim 10\ \ell_B^{-1}$, which occurs at $\varphi = \pi/4$ where V_s is minimal. We therefore expected isopotential drift behaviour $v = \alpha\omega_c\ell_B$ for $\alpha \lesssim k_{\max}\ell_B \approx 10$, shown by a dotted line, and a hard wall speed $v = \hbar k_{\max}/m \approx 10\omega_c\ell_B$ for $\alpha \gtrsim 10$, in excellent agreement with the experiment.

Classically, this behaviour can be understood as a crossover from the $\mathbf{E} \times \mathbf{B}$ drift of cyclotron orbits subjected to a uniform force to skipping motion along a hard boundary. This occurs when the force arising from the wall $F_{\mathrm{wall}} = \alpha\hbar\omega_c/\ell_B$ becomes comparable to the Coriolis force towards the wall $F_{\mathrm{Coriolis}} \approx \hbar k_{\max}\omega_c$. The ratio of these quantities is shown on the top x axis in Fig. 3b.

For a more quantitative comparison we analytically solved the Schrödinger equation in the case of a linear wall and obtained the edge mode dispersion relation (Methods). For each wall steepness we obtained $k_{\max}$ and the associated group velocity, which is shown by the solid black curve in Fig. 3b and captures the data well without any free parameters. We also indicate (using blue triangles) the speed obtained from a Gross–Pitaevskii simulation of our experiment. In the inset of Fig. 3b we show the ground bands of the theoretical dispersion relation for different values of α, which do deviate from the hard wall result and instead vary linearly $E_0(k) \approx \alpha\hbar\omega_c\ell_B k$ when $k\ell_B \gtrsim \alpha$.

https://doi.org/10.1038/s41567-024-02617-7

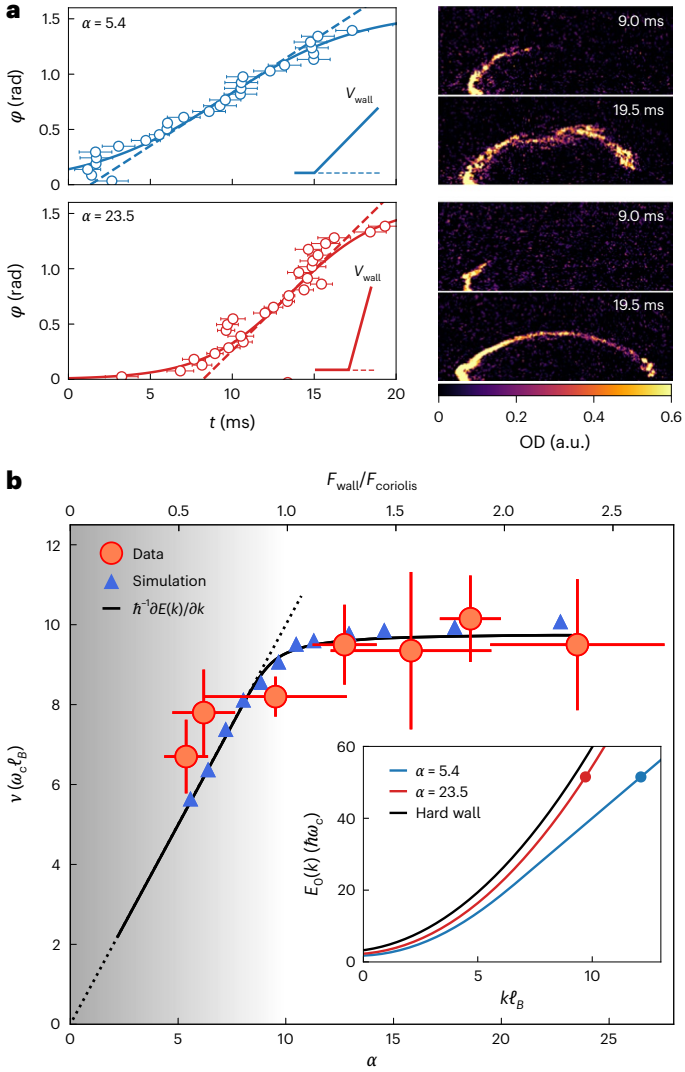

Fig. 3 | Variation in edge mode speed with wall steepness. a, Temporal evolution of the edge mode azimuthal position for two values of wall steepness α (left) and corresponding images of the atomic densities (right). We fitted these data with a sigmoid function (solid line) whose central slope (dashed line) corresponds to the angular speed at the peak wavevector k_{max}. **b**, Edge mode speed as a function of wall steepness, which exhibits a crossover between isopotential drift behaviour $v = \alpha\omega_c\ell_B$ (dotted line) in the limit $\alpha \lesssim k_{max}\ell_B \approx 10$ (grey region) and a constant value for steeper walls consistent with the chiral free-particle result $\hbar k_{max}/m \approx 10\,\omega_c\ell_B$. The solid black line shows the group velocity obtained from the theoretical dispersion relation associated with a wall of finite steepness. The inset shows the dispersion relation itself, where solid points indicate the maximum injected wavevector for each steepness. Error bars in all plots indicate 1σ.

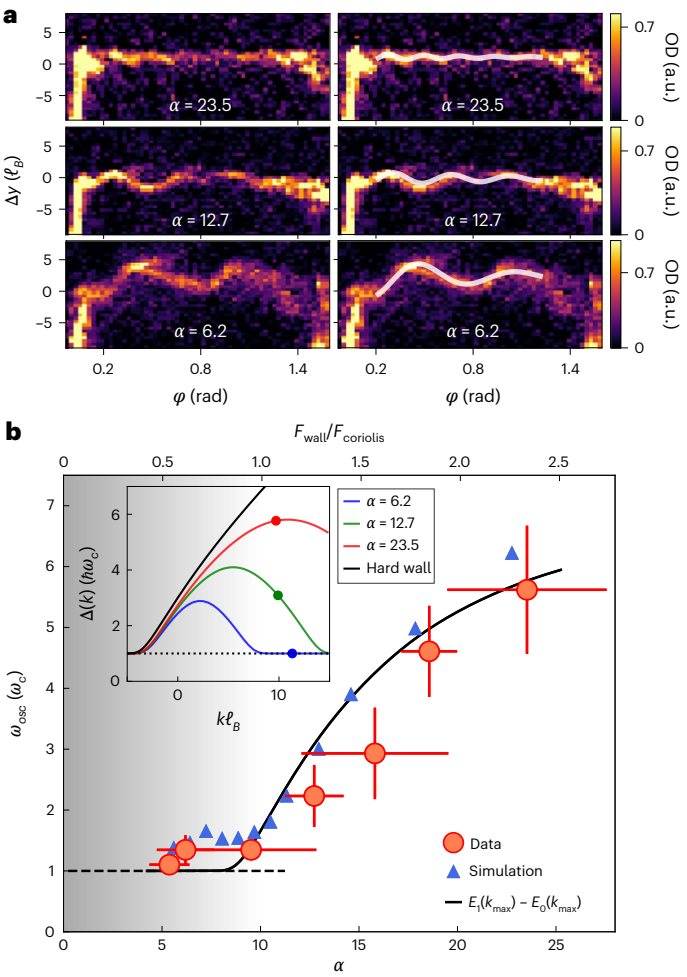

Fig. 4 | Frequency of skipping orbits at the boundary. a, Edge mode density profiles as a function of azimuthal angle and radial distance relative to the wall, Δy, for various α. The density exhibits a dipole oscillation due to excitation of the first excited edge band, which is fitted with a damped sinusoid (white line, plotted for clarity on the right-hand duplicate of each image). **b**, From the measured oscillation period and edge mode speed, we infer the temporal oscillation frequency ω_{osc}. This is shown by red data points, and exhibits a monotonic increase with α relative to the Landau level splitting $\hbar\omega_c$, which is recovered in the limit of shallow walls (grey region). Error bars indicate 1σ. In the inset we show the theoretical energy gap $\Delta(k)$ between the ground and first excited edge band, which deviates from its bulk value (dotted line) in the range $0 \lesssim k\ell_B \lesssim \alpha$. The data points indicate $\Delta(k_{max})$, which is shown in the main plot by a solid black line without any free parameters.

Accompanying this crossover from isopotential drift physics to hard wall behaviour, we anticipated an associated change in the energy gap between different bands in the dispersion relation. To infer this splitting, we exploited a small residual excitation of the first excited band in our experiment, which resulted in a dipole oscillation of the edge mode centre of mass at a frequency $\Delta(k)/\hbar = (E_1(k) - E_0(k))/\hbar$. We attribute this excitation to the short timescale $4\ell_B/(\varepsilon\omega_c R) \approx 0.1 \times 2\pi/\omega_c$, much less than one cyclotron period, over which a wavepacket of approximate extent ℓ_B moving radially along the saddle diagonal at a speed $\varepsilon\omega_c r/4$ (ref. 41) encounters the edge. The spatial amplitude of the radial oscillations is approximately 0.2 µm, or equivalently $0.1\ell_B$. From theoretical knowledge of the wavefunctions of different bands (Methods), we estimated an approximately 10% admixture of the first excited band.

In Fig. 4a we show the edge mode density as a function of azimuthal angle and radial distance relative to R. Similarly to Fig. 3, the saddle potential was continually present for these measurements. The centre of mass exhibited an oscillation that increased in amplitude with decreasing α; we attributed this to the greater spatial extent of the associated edge mode wavefunctions. We extracted the radial position of the edge mode, the azimuthal variation of which was fitted with a damped sinusoid of period $\delta\varphi$, shown by white lines. Together with the maximal speed of atoms, v, attained at $\varphi = \pi/4$ and presented in Fig. 3, we obtained the temporal oscillation frequency $\omega_{osc} \approx 2\pi v/(R\delta\varphi)$, which is shown in Fig. 4b.

For shallow walls, ω_{osc} is consistent with the cyclotron frequency (dotted line in Fig. 4b), indicating that the edge bands are split by their bulk value. However, ω_{osc} increases for $\alpha \gtrsim k_{max}\ell_B \approx 10$ (indicating that the edge mode wavefunction is sampling the wall onset), resulting in a quantum mechanical analogue of classical skipping motion, the

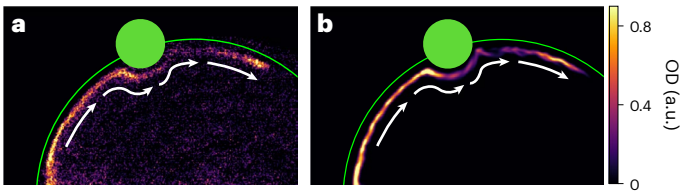

Fig. 5 | Robustness of edge modes against disorder. a, We created an obstacle at the boundary by projecting a repulsive Gaussian beam. The atoms flow smoothly around the wall deformation without any discernible backscattering. **b**, A Gross–Pitaevskii simulation of the same experimental sequence, exhibiting the same robust propagation.

frequency of which exceeds that of the bulk cyclotron orbits. For comparison, the solid black line shows the frequency $\Delta(k)/\hbar$ obtained from the theoretical dispersion relation and captures the data well. In the inset of Fig. 4b we show $\Delta(k)$ for walls of varying steepness, illustrating its deviation from the bulk Landau level splitting for wavevectors $0 \lesssim k\ell_B \lesssim \alpha$.

The chirality of edge modes means that particle propagation is robust against boundary imperfections. To demonstrate this, we created an obstacle by projecting a Gaussian laser beam with a radius of ~$10\ell_B$ coincident with the system boundary, which co-rotated with our magnetic trap such that the resulting repulsive potential was static in the rotating frame. As shown in Fig. 5, the atoms flowed smoothly around the obstacle. We also show the result of a Gross–Pitaevskii simulation of the same experiment, obtaining the same behaviour.

These observations demonstrate the realization of chiral edge modes in a rapidly rotating ultracold gas, revealing their speed, structure, bandgap, dependence on wall sharpness and robustness against disorder. A natural immediate direction of future work concerns the influence of disorder length scale and dynamics. Furthermore, this approach provides a platform for addressing the role of interactions. One particular advantage of using rotating gases is that the interactions between atoms are decoupled from the induced gauge potential, in contrast to other methods for which the effective magnetic field appears within a dressed-atom picture[48]. In our bosonic system, one anticipates the formation of a chiral Lieb–Liniger gas at the boundary[49,50]. More broadly, edge modes naturally constitute one-dimensional channels with a speed that is either proportional to, or independent of, the confining force, in contrast to inertial frames in which forces yield acceleration. This may enable robust atomic waveguides in analogy to electronic interferometers formed by quantum Hall edge states[51,52].

Note added in proof: During the typesetting of this manuscript, we became aware of a related work realizing edge modes in a Floquet lattice system[53].

Online content

Any methods, additional references, Nature Portfolio reporting summaries, source data, extended data, supplementary information, acknowledgements, peer review information; details of author contributions and competing interests; and statements of data and code availability are available at https://doi.org/10.1038/s41567-024-02617-7.

References

1. Klitzing, K. V., Dorda, G. & Pepper, M. New method for high-accuracy determination of the fine-structure constant based on quantized Hall resistance. *Phys. Rev. Lett.* **45**, 494 (1980).
2. Laughlin, R. B. Quantized Hall conductivity in two dimensions. *Phys. Rev. B* **23**, 5632 (1981).
3. Halperin, B. I. Quantized Hall conductance, current-carrying edge states, and the existence of extended states in a two-dimensional disordered potential. *Phys. Rev. B* **25**, 2185 (1982).
4. Jackiw, R. & Rebbi, C. Solitons with fermion number 1/2. *Phys. Rev. D* **13**, 3398 (1976).
5. Thouless, D. J., Kohmoto, M., Nightingale, M. P. & den Nijs, M. Quantized Hall conductance in a two-dimensional periodic potential. *Phys. Rev. Lett.* **49**, 405 (1982).
6. Hatsugai, Y. Chern number and edge states in the integer quantum Hall effect. *Phys. Rev. Lett.* **71**, 3697 (1993).
7. Hasan, M. Z. & Kane, C. L. Colloquium: topological insulators. *Rev. Mod. Phys.* **82**, 3045 (2010).
8. Stormer, H. L., Tsui, D. C. & Gossard, A. C. The fractional quantum Hall effect. *Rev. Mod. Phys.* **71**, S298 (1999).
9. Sinova, J., Valenzuela, S. O., Wunderlich, J., Back, C. H. & Jungwirth, T. Spin Hall effects. *Rev. Mod. Phys.* **87**, 1213 (2015).
10. Lu, L., Joannopoulos, J. D. & Soljacic, M. Topological photonics. *Nat. Photon.* **8**, 821–829 (2014).
11. Read, N. & Green, D. Paired states of fermions in two dimensions with breaking of parity and time-reversal symmetries and the fractional quantum Hall effect. *Phys. Rev. B* **61**, 10267 (2000).
12. Sato, M. & Ando, Y. Topological superconductors: a review. *Rep. Prog. Phys.* **80**, 076501 (2017).
13. Büttiker, M. Absence of backscattering in the quantum Hall effect in multiprobe conductors. *Phys. Rev. B* **38**, 9375 (1988).
14. Chklovskii, D. B., Shklovskii, B. I. & Glazman, L. I. Electrostatics of edge channels. *Phys. Rev. B* **46**, 4026 (1992).
15. Chamon, Cd. C. & Wen, X. G. Sharp and smooth boundaries of quantum Hall liquids. *Phys. Rev. B* **49**, 8227 (1994).
16. Kane, C. L. & Fisher, M. P. A. Impurity scattering and transport of fractional quantum Hall edge states. *Phys. Rev. B* **51**, 13449 (1995).
17. Kane, C. L. & Fisher, M. P. A. Quantized thermal transport in the fractional quantum Hall effect. *Phys. Rev. B* **55**, 15832 (1997).
18. Grayson, M., Tsui, D. C., Pfeiffer, L. N., West, K. W. & Chang, A. M. Continuum of chiral Luttinger liquids at the fractional quantum Hall edge. *Phys. Rev. Lett.* **80**, 1062 (1998).
19. Wan, X., Yang, K. & Rezayi, E. H. Reconstruction of fractional quantum Hall edges. *Phys. Rev. Lett.* **88**, 056802 (2002).
20. Yacoby, A., Hess, H., Fulton, T., Pfeiffer, L. & West, K. Electrical imaging of the quantum Hall state. *Solid State Commun.* **111**, 1–13 (1999).
21. Aoki, N., da Cunha, C. R., Akis, R., Ferry, D. K. & Ochiai, Y. Imaging of integer quantum Hall edge state in a quantum point contact via scanning gate microscopy. *Phys. Rev. B* **72**, 155327 (2005).
22. Lai, K. et al. Imaging of Coulomb-driven quantum Hall edge states. *Phys. Rev. Lett.* **107**, 176809 (2011).
23. Suddards, M. E., Baumgartner, A., Henini, M. & Mellor, C. J. Scanning capacitance imaging of compressible and incompressible quantum Hall effect edge strips. *New J. Phys.* **14**, 083015 (2012).
24. Uri, A. et al. Nanoscale imaging of equilibrium quantum Hall edge currents and of the magnetic monopole response in graphene. *Nat. Phys.* **16**, 164–170 (2019).
25. Ashoori, R. C., Stormer, H. L., Pfeiffer, L. N., Baldwin, K. W. & West, K. Edge magnetoplasmons in the time domain. *Phys. Rev. B* **45**, 3894 (1992).
26. Bid, A. et al. Observation of neutral modes in the fractional quantum Hall regime. *Nature* **466**, 585–590 (2010).
27. Johnsen, T. et al. Mapping quantum Hall edge states in graphene by scanning tunneling microscopy. *Phys. Rev. B* **107**, 115426 (2023).
28. Dalibard, J., Gerbier, F., Juzeliūnas, G. & Öhberg, P. Colloquium: artificial gauge potentials for neutral atoms. *Rev. Mod. Phys.* **83**, 1523 (2011).
29. Goldman, N., Juzeliūnas, G., Öhberg, P. & Spielman, I. B. Light-induced gauge fields for ultracold atoms. *Rep. Prog. Phys.* **77**, 126401 (2014).
30. Galitski, V. & Spielman, I. B. Spin–orbit coupling in quantum gases. *Nature* **494**, 49–54 (2013).

31. Chalopin, T. et al. Probing chiral edge dynamics and bulk topology of a synthetic Hall system. *Nat. Phys.* **16**, 1017–1021 (2020).
32. Struck, J. et al. Tunable gauge potential for neutral and spinless particles in driven optical lattices. *Phys. Rev. Lett.* **108**, 225304 (2012).
33. Jotzu, G. et al. Experimental realization of the topological Haldane model with ultracold fermions. *Nature* **515**, 237–240 (2014).
34. Aidelsburger, M. et al. Measuring the Chern number of Hofstadter bands with ultracold bosonic atoms. *Nat. Phys.* **11**, 162–166 (2015).
35. Stuhl, B. K., Lu, H.-I., Aycock, L. M., Genkina, D. & Spielman, I. B. Visualizing edge states with an atomic Bose gas in the quantum Hall regime. *Science* **349**, 1514–1518 (2015).
36. Mancini, M. et al. Observation of chiral edge states with neutral fermions in synthetic Hall ribbons. *Science* **349**, 1510–1513 (2015).
37. Tai, M. E. et al. Microscopy of the interacting Harper–Hofstadter model in the two-body limit. *Nature* **546**, 519–523 (2017).
38. Schweikhard, V., Coddington, I., Engels, P., Mogendorff, V. P. & Cornell, E. A. Rapidly rotating Bose–Einstein condensates in and near the lowest Landau level. *Phys. Rev. Lett.* **92**, 040404 (2004).
39. Bretin, V., Stock, S., Seurin, Y. & Dalibard, J. Fast rotation of a Bose–Einstein condensate. *Phys. Rev. Lett.* **92**, 050403 (2004).
40. Cooper, N. R. Rapidly rotating atomic gases. *Adv. Phys.* **57**, 539–616 (2008).
41. Fletcher, R. J. et al. Geometric squeezing into the lowest Landau level. *Science* **372**, 1318–1322 (2021).
42. Mukherjee, B. et al. Crystallization of bosonic quantum Hall states in a rotating quantum gas. *Nature* **601**, 58–62 (2022).
43. Ho, T. L. Bose–Einstein condensates with large number of vortices. *Phys. Rev. Lett.* **87**, 060403 (2001).
44. Bouhiron, J.-B. et al. Realization of an atomic quantum Hall system in four dimensions. *Science* **384**, 223–227 (2024).
45. Wen, X.-G. Topological orders and edge excitations in fractional quantum Hall states. *Adv. Phys.* **44**, 405–473 (1995).
46. Petrich, W., Anderson, M. H., Ensher, J. R. & Cornell, E. A. Stable, tightly confining magnetic trap for evaporative cooling of neutral atoms. *Phys. Rev. Lett.* **74**, 3352 (1995).
47. Bièvre, S. D. & Pulé, J. V. Propagating edge states for a magnetic Hamiltonian. *Math. Phys. Electron. J.* **5**, 39–55 (2002).
48. Bukov, M., D'Alessio, L. & Polkovnikov, A. Universal high-frequency behavior of periodically driven systems: from dynamical stabilization to Floquet engineering. *Adv. Phys.* **64**, 139 (2015).
49. Lieb, E. H. & Liniger, W. Exact analysis of an interacting Bose gas. I. The general solution and the ground state. *Phys. Rev.* **130**, 1605–1616 (1963).
50. Sinha, S. & Shlyapnikov, G. V. Two-dimensional Bose–Einstein condensate under extreme rotation. *Phys. Rev. Lett.* **94**, 150401 (2005).
51. Ji, Y. et al. An electronic Mach–Zehnder interferometer. *Nature* **422**, 415–418 (2003).
52. Zhang, Y. et al. Distinct signatures for Coulomb blockade and Aharonov-Bohm interference in electronic Fabry-Pérot interferometers. *Phys. Rev. B* **79**, 241304 (2009).
53. Braun, C. et al. Real-space detection and manipulation of topological edge modes with ultracold atoms. *Nat. Phys.* **20**, 1306–1312 (2024).

Publisher's note Springer Nature remains neutral with regard to jurisdictional claims in published maps and institutional affiliations.

Springer Nature or its licensor (e.g. a society or other partner) holds exclusive rights to this article under a publishing agreement with the author(s) or other rightsholder(s); author self-archiving of the accepted manuscript version of this article is solely governed by the terms of such publishing agreement and applicable law.

© The Author(s), under exclusive licence to Springer Nature Limited 2024

Methods

Imaging set-up

Images of the cloud density are broadened by both optical diffraction and atomic diffusion during the imaging pulse. This was previously calibrated in ref. 41, and the effective broadening of a point source by our system was captured via convolution by a Gaussian function with a $e^{-1/2}$ radius of 670 nm. For comparison, this performance was sufficient to observe vortices in situ with a contrast of ~60% (ref. 41). These have a characteristic size set by the healing length, which is ~300 nm in our system. This is smaller than the spatial extent of the edge modes, set by the rotational analogue of the magnetic length, $\ell_B = \sqrt{\hbar/(m\omega_c)} = 1.6\,\mu\text{m}$.

Calibration of the wall steepness

To calibrate the effective wall steepness, we directly imaged the intensity pattern projected onto the atoms using a microscope objective with a numerical aperture of 0.5. We then identified the azimuthal position where atoms transitted the region of minimum saddle potential, and thus where the edge mode speed was maximal, and extracted the corresponding radial intensity profile $I(r)$. We fitted the radial intensity profile to an error function, which we then deconvolved with the known point spread function of the microscope objective to obtain the intensity pattern at the atoms themselves.

This inferred profile was then fitted with a piecewise linear function:

$$I(r) = \begin{cases} 0, & r < c_1 \\ c_2(r - c_1), & c_1 < r < c_1 + 1/c_2 \\ 1, & r > c_1 + 1/c_2. \end{cases} \tag{2}$$

Here, c_1 and c_2 are fit parameters. Combined with the known projected potential height, V_0, we inferred the potential slope $\alpha = V_0 c_2 \ell_B/(\hbar\omega_c)$ used in the main text. This protocol ensured that we always obtained the wall steepness corresponding to the location of minimum saddle potential and maximal edge mode speed even if there was any variation in steepness with azimuthal position. Two examples of this wall steepness extraction are shown in Extended Data Fig. 1.

Dispersion relation associated with a piecewise linear wall potential

For the wall defined in the main text, it was convenient to work in the Landau gauge and label eigenstates $\psi_k(y)$ by their momentum k along the wall, giving a Hamiltonian:

$$\hat{H}_k = \frac{\hat{p}_y^2}{2m} + \frac{1}{2}m\omega_c^2(\hat{y} - k\ell_B^2)^2 + \alpha\frac{\hbar\omega_c}{\ell_B}\hat{y}\,\Theta(\hat{y}) \tag{3}$$

where $\Theta(\hat{y})$ is the Heaviside function. Below we drop hats on operators for simplicity. We define dimensionless variables $\tilde{y} = y/\ell_B$, $\tilde{k} = k\ell_B$ and energy $\tilde{E}(\tilde{k}) = E(k)/\hbar\omega_c$, yielding a dimensionless Schrödinger equation:

$$\left[-\frac{1}{2}\partial_{\tilde{y}}^2 + \frac{1}{2}(\tilde{y} - \tilde{k})^2 + \alpha\tilde{y}\,\Theta(\tilde{y})\right]\psi_{\tilde{k}}(\tilde{y}) = \tilde{E}(\tilde{k})\psi_{\tilde{k}}(\tilde{y}) \tag{4}$$

For either $\tilde{y} > 0$ or $\tilde{y} < 0$, this coincides with the Weber equation[54], whose solutions are linear combinations of hyperbolic cylinder functions $D_\nu(z)$. Normalizability of the wavefunction requires that the single-particle eigenstates take the piecewise differentiable form: $\psi_{\tilde{k}}(\tilde{y}) = A_{<0}D_{\tilde{E}(\tilde{k})-1/2}(-\sqrt{2}(\tilde{y} - \tilde{k}))$ for $\tilde{y} < 0$, and $\psi_{\tilde{k}}(\tilde{y}) = A_{>0}D_{\tilde{E}(\tilde{k})+(\tilde{k}-\alpha)^2/2-\tilde{k}^2/2-1/2}(\sqrt{2}(\tilde{y} - \tilde{k} + \alpha))$ for $\tilde{y} > 0$. By matching both the value and gradient of ψ at $\tilde{y} = 0$, we obtained the dispersion relation. In the case of a hard wall, we used the simpler boundary condition $\psi_{\tilde{k}}(\tilde{y} \to 0^-) = 0$ without consideration of the region $\tilde{y} > 0$ (ref. 47).

In the presence of the saddle potential, this dispersion relation is slightly modified owing to an additional force towards the wall $F = \frac{\varepsilon\hbar\omega_c R\sin(2\varphi)}{4\ell_B^2} \equiv \tilde{F}(\varphi)\hbar\omega_c/\ell_B$. The Hamiltonian (3) therefore acquires an additional term $-F\hat{\mathbf{y}}$, and the modified dispersion relation $\tilde{E}_n^{(F)}(\tilde{k})$ is related to the case of no saddle potential by $\tilde{E}_n^{(F)}(\tilde{k}) = \tilde{E}_n(\tilde{k} - \tilde{F}) + \tilde{F}\tilde{k} - \frac{1}{2}\tilde{F}^2$ (ref. 31).

The wavevector $\mathbf{k}$ of an atom in the lowest edge band, propagating in the presence of the saddle potential, is determined by the energy conservation requirement:

$$\frac{\varepsilon\hbar\omega_c}{8}\left(\frac{R}{\ell_B}\right)^2\sin(2\varphi) + \frac{\hbar\omega_c}{2} = E_0^{(F)}(k), \tag{5}$$

where $\hbar\omega_c/2$ is the band energy in the bulk where $\tilde{F} = 0$, corresponding to the lowest Landau level energy.

Simulation of the Gross–Pitaevskii equation

We performed further numerical simulations of our experiment via time evolution of the Gross–Pitaevskii equation. We began with an equilibrated, weakly interacting Bose–Einstein condensate in a static anisotropic harmonic trap with same trap frequencies and condensate chemical potential as our experiment. The wall potential was modelled via the piecewise linear function of equation (2), with $c_1 = 90\,\mu\text{m}$ and variable steepness. We evolved the condensate wavefunction under an identical sequence to that performed in the experiment, and extracted the speed of the edge modes and the azimuthal period of their radial oscillations via identical analysis. A time series of exemplary images is shown in Extended Data Fig. 2.

Extraction of wavefront position and speed

To obtain the dynamics of the atomic wavefront, we divided the edge into azimuthal bins and plotted the total number of atoms within each bin as a function of time. These data were fitted with a sigmoid function to extract the time at which the number of atoms increased to 50% of the steady-state value. This time was then plotted against the corresponding bin angle to obtain the evolution of the wavefront position $\varphi(t)$; examples are shown in Fig. 3a. The error bars associated with the velocities shown in Figs. 1d and 3b are fitting errors from extracting the edge mode speed from the data $\varphi(t)$.

Creation of the optical boundary

The optical boundary was formed by imaging 532 nm light incident on a digital micromirror device (DMD) onto the atoms. The pixel diameter on the DMD was 7.6 μm, the magnification of the imaging system was 27.8 and the numerical aperture of the projection objective was 0.5. This resulted in an optical point spread function with a full-width at half-maximum of 550 nm and one pixel of the DMD corresponded to 270 nm at the atoms. Both length scales are much smaller than $\ell_B \approx 1.6\,\mu\text{m}$, which set the natural physics length scale. The shape of the wall was optimized by maximizing the spin-down time of a rotating condensate that contained an Abrikosov lattice of vortices confined within the wall potential using a smaller ring of radius 30 μm. Ring centring was performed by projecting a small beam formed by turning on a few pixels at the centre of the DMD pattern and making a hole at the centre of a non-rotating condensate. Once optimized, this spin-down time of the cloud was several seconds—much longer than the timescale of any of the experiments presented here.

Creation of the optical obstacle

The obstacle was formed by a beam of 532 nm light that first passed through a two-axis acousto-optical deflector and was then focused to a 20 μm waist at the atoms. The resulting repulsive potential had a peak value of $40\hbar\omega_c$. By modulating the deflection angle along each axis at a frequency corresponding to the atomic rotation, we induced the focal spot to travel along our circular wall such that in the rotating frame it appeared static. The beam was also sampled before the projection objective to confirm the uniformity of the power during one rotation cycle.

Data availability

All data files are available from the corresponding author upon request. Accompanying data, including data for Figs. 1–5 and Extended Data Figs. 1 and 2 are available via Zenodo at https://doi.org/10.5281/zenodo.12724216 (ref. 55).

Code availability

The simulation and analysis code is available from the corresponding author upon reasonable request.

References

54. Fernández, F. M. Simple one-dimensional quantum-mechanical model for a particle attached to a surface. *Eur. J. Phys.* **31**, 961 (2010).
55. Yao, R. et al. Observation of chiral edge transport in a rapidly-rotating quantum gas. *Figshare* https://doi.org/10.5281/zenodo.12724216 (2024).

Acknowledgements

We thank V. Crépel, P. Patel, C. Wilson and Z. Yan for early contributions to the experiment. This work was supported by the NSF through the Center for Ultracold Atoms and grant number PHY-2012110, the ARO through grant number W911NF-23-1-0382 and by DURIP grant number W911NF-23-1-0326. M.Z. acknowledges funding from the Vannevar Bush Faculty Fellowship (ONR number N00014-19-1-2631). R.J.F. acknowledges funding from the AFOSR Young Investigator Program (grant number FA9550-22-1-0066).

Author contributions

R.Y., S.C., B.M., A.S. and R.J.F. performed the measurements. R.Y. and S.C. analysed the data. B.M. and R.Y. contributed the Gross–Pitaevskii numerical simulations. R.Y., S.C., R.J.F. and M.Z. developed the theoretical description. R.J.F. and M.Z. supervised the project. All authors contributed to interpretation of the results and preparation of the manuscript.

Competing interests

The authors declare no competing interests.

Additional information

Extended data is available for this paper at https://doi.org/10.1038/s41567-024-02617-7.

Correspondence and requests for materials should be addressed to Richard J. Fletcher.

Peer review information *Nature Physics* thanks Luca Asteria for his contribution to the peer review of this work.

Reprints and permissions information is available at www.nature.com/reprints.

https://doi.org/10.1038/s41567-024-02617-7

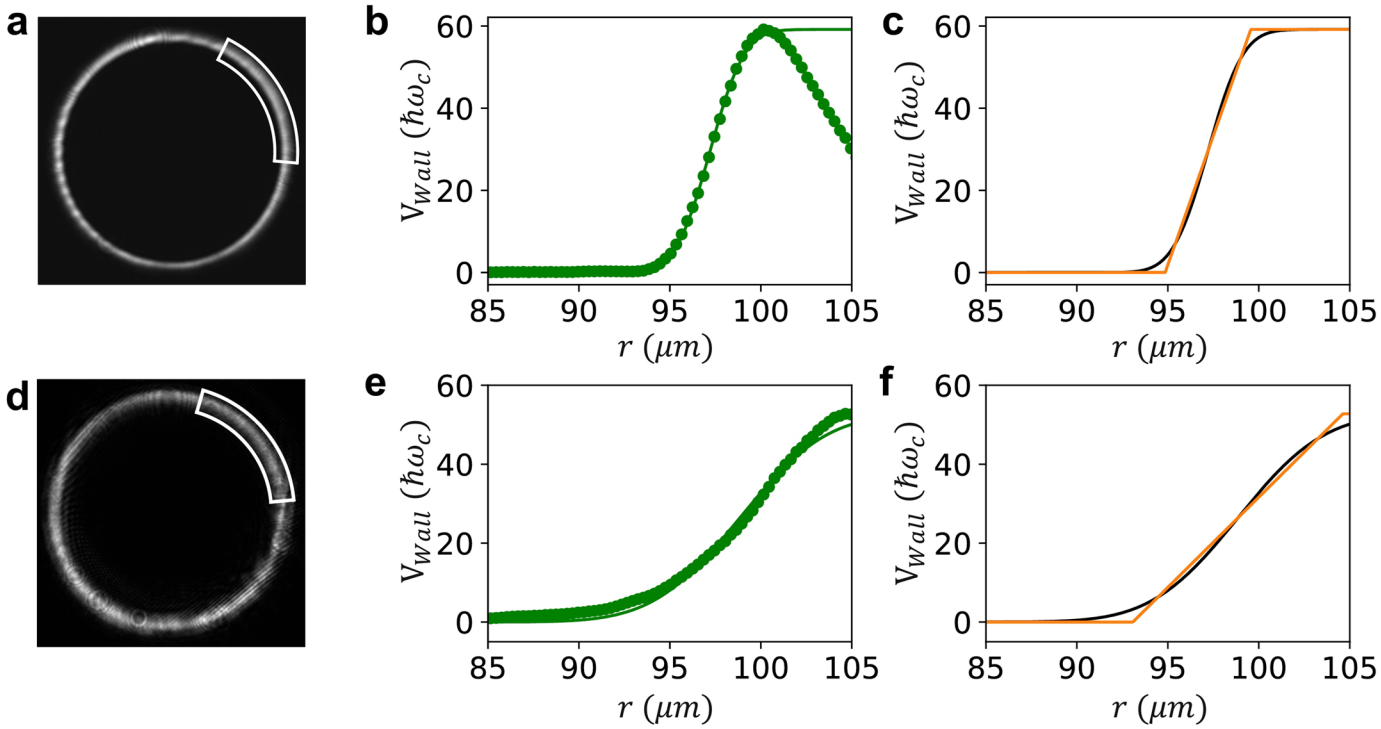

Extended Data Fig. 1 | Analysis of the boundary potential. (**a**,**d**) Images of the projected optical boundary. The white boxes indicate the approximate azimuthal range explored by the atoms as they pass through the saddle minimum, and hence the edge mode speed is maximum. (**b**,**e**) The measured radial intensity $I(r)$, averaged over the indicated range of azimuthal angles. The green line shows a fitted error function. (**c**,**f**) The black curve is the inferred intensity profile at the atoms, obtained by de-convolution of the green curve in (**b**,**e**). The orange line is a piecewise linear fit to the black curve, whose slope provides the effective steepness of the boundary potential.

https://doi.org/10.1038/s41567-024-02617-7

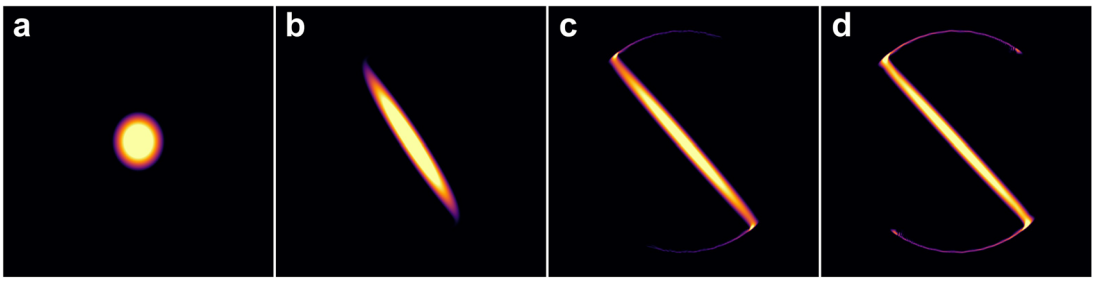

Extended Data Fig. 2 | Evolution of the condensate density obtained from a Gross-Pitaevskii simulation. We perform a numerical simulation of the condensate evolution based on time-evolution of the Gross-Pitaevskii equation under an identical protocol to the experiment. Panels show the condensate density (**a**) before rotation; (**b**) when $\Omega = 0.85\omega$; (**c**) once $\Omega = \omega$, approximately corresponding to the time at which the condensate encounters the edge potential; (**d**) after 5ms of edge mode propagation.